

Continuum description of confluent tissues with spatial heterogeneous activity

Fernanda Pérez-Verdugo ^{*a} and Rodrigo Soto ^b

A continuum description is built to characterize the stationary and transient deformations of confluent tissues subject to heterogeneous activities. By defining a coarse-grained texture matrix field to represent the shape and size of cells, we derive the coarse-grained stress tensor for the vertex model. Activity in the tissue takes the form of inhomogeneous apical contractions, which can be modeled as reductions of the vertex model reference areas or perimeters representing activity in the medial and perimeter regions of the cells, respectively. For medial activity, the extra stress is just an isotropic pressure, while for perimeter activity, it also has a deviatoric component, which is aligned with the texture matrix. The predictions of the continuum description are compared with the average spatiotemporal deformations obtained in simulations of the vertex model subject to localized apical contractions, showing an excellent agreement, even if the active patch is as small as one cell. The fluctuations around the average are more prominent when the activity is in the medial region due to the lack of negative active shape feedback, which, coupled with the confluent property, increases cellular shape and size variations.

1 Introduction

Heterogeneity is detected across all scales in biological systems, from cellular components to organs. Variations in morphology^{1,2}, expression levels³, and function² are particularly observed across cells within a tissue. For a long time, the average response has been researched as a representation of these systems. Yet recent studies have emphasized the biological significance of heterogeneity in various facets, such as cancer^{4,5}, epithelial wound healing⁶, and cell competition⁷, highlighting the need for comprehensive knowledge and measurements of (population, temporal, and spatial) variations in biological systems⁸.

Non-genetic heterogeneity, also known as phenotypic heterogeneity, can be induced by extrinsic and intrinsic variables in epithelial tissues⁸, and has been associated with changes in cell-level mechanical properties^{6,9}. Variations in cellular adhesion and contractility specifically govern cell sorting or mixing⁹. In the context of cancer, heterogeneity is of special importance since intratumor areas exhibit high morphological variations linked with adaptation and resistance to therapy, hence promoting disease progression^{4,5}.

Some recent cell-level computational and continuum models account for tissue heterogeneities^{7,9,10}. Specifically, in Ref. ⁷, the authors analyzed population heterogeneity in relation to mechanical heterogeneity using a cell-level model, showing that vari-

ations in the cellular shape index (defined as the ratio of the preferred perimeter to the square root of the preferred area) increase tissue-level rigidity. Similarly, in Ref. ¹¹, we considered mechanical heterogeneities, localized in space and time, as active processes associated with internal changes at specific cellular regions, medial and periphery, resulting in variations in the cellular shape index. Thus, we were able to make quantitative predictions on the stress localization based on the observed experimental cellular morphologies. The intermediate spatial scale of these inhomogeneous activities, which are directly linked to large-scale mechanical inhomogeneities, has not been studied using numerical simulations or continuous models.

In this paper, we present a continuum description for confluent tissues in the absence of cellular rearrangements, exhibiting spatially inhomogeneous cellular activity that is directly related to mechanical heterogeneities. The continuum theory is founded on a coarse-grained expression for the tissue stresses, derived from the vertex model, as previously reported in Ref. ¹², with a direct mapping between the cell-level and continuum parameters. We compare the outcomes of the continuum description with numerical simulations employing the vertex model under various scenarios where activity causes inhomogeneous cellular contractions exhibiting fluidity or solidity geometrical features. Even for active regions as small as one cell, the agreement between the two descriptions is excellent. Our validated continuous model offers a substantial analytical and numerical advantage. It allows, for example, the direct inclusion of spatial symmetries that describe the tissue dynamics, such as during the formation of the ventral

^a Department of Physics, Carnegie Mellon University, Pittsburgh, PA 15213, USA.

E-mail: fverdugo@andrew.cmu.edu

^b Departamento de Física, FCFM, Universidad de Chile, Santiago, Chile.

furrow formation in *Drosophila*^{13,14}, and the neural tube in *Xenopus*¹⁵. We finally discuss the effect of intrinsic disorder in the tissue, included as a population heterogeneity in numerical simulations (as in Ref.⁷), on the fluctuations of the microscopic model around the predictions of the continuum description.

2 Continuum description of the vertex model

The two-dimensional vertex model^{16,17} has been demonstrated to be both qualitatively and quantitatively adequate for describing the dynamics of morphogenic processes in confluent tissues^{18–20}. In this model, each cell c is represented by a polygon with area A_c (target area A_{0c}) and perimeter P_c (target perimeter P_{0c}). The position of the vertex \mathbf{r}_i follows a variational dynamics, $\mu d\mathbf{r}_i/dt = -\partial E/\partial \mathbf{r}_i$, where μ is the friction coefficient, and E is an energy function given by

$$E = \frac{K_A}{2} \sum_c (A_c - A_{0c})^2 + \frac{K_P}{2} \sum_c (P_c - P_{0c})^2 + J \sum_{\langle i,j \rangle} l_{ij}. \quad (1)$$

The first and second sums run over all the cells and penalize deviations of areas and perimeters, with elastic modulus K_A and K_P , respectively. The third sum is taken over the adjacent vertices i and j , joined by a cell junction of length l_{ij} under a constant line tension J . Although it is possible to absorb the constant line tension J into the perimeter penalization term, we keep all three terms as in Ref.²¹, and directly denominate medial (perimeter) activity to spatial variations of A_{0c} (P_{0c}).

A useful way to characterize the shape of a cell c , made of n_c vertices with positions \mathbf{r}_i , is given by the symmetric texture tensor

$$\mathbb{M}_c = \frac{2}{n_c} \sum_{i \in c} (\mathbf{r}_i - \mathbf{r}_c) \otimes (\mathbf{r}_i - \mathbf{r}_c), \quad (2)$$

where \mathbf{r}_c is the centroid of the cell c ²². For a regular hexagon, \mathbb{M}_c is equal to $R_{\text{out}}^2 \mathbb{1}$, where R_{out} corresponds to the circumscribed circle and $\mathbb{1}$ is the identity matrix. For a rhombus of diagonals $2a$ and $2b$, with $a > b$ (low-resolution version of an ellipse of semi-axis a and b), the eigenvalues of \mathbb{M}_c are a^2 and b^2 , and the eigenvectors give the orientations of each diagonal. In general, the area and perimeter of the cell c can be written as $A_c = c_1 \sqrt{\det \mathbb{M}_c}$ and $P_c = c_2 \sqrt{\text{tr} \mathbb{M}_c}$, where c_1 and c_2 depend on the type of polygon. In particular, for the previous hexagon and rhombus, $c_1 = \{3\sqrt{3}/2, 2\}$ and $c_2 = \{3\sqrt{2}, 4\}$, respectively. For a hexagon of initial side R , under a pure shear deformation of amplitude ε , the previous expression for the perimeter is corrected by $-3R\varepsilon^2/2 + \mathcal{O}(\varepsilon^4)$, and the area by $-3\sqrt{3}R^2\varepsilon^2 + \mathcal{O}(\varepsilon^4)$. For a square (a particular case of rhombus) of initial side R , under a horizontal expansion of amplitude ε (rectangle of sides R and $R(1+\varepsilon)$), the correction for the perimeter is $-R\varepsilon^2/2 + \mathcal{O}(\varepsilon^3)$, while there is no correction for the area. Other deformations produce similar results. As a consequence, the previous expressions for A_c and P_c give the correct values to the dominant order, allowing us to use them in a continuous description.

We consider a coarse-graining over the discrete perspective of the tissue in order to obtain a smooth, symmetric tensor field $\mathbb{M}(\mathbf{r})$, which now reflects shape at a tissue scale. Therefore, as shown in Refs.¹², under a displacement field \mathbf{u} , the tensor field \mathbb{M}

will be modified (up to $O(|\nabla \mathbf{u}|)$) as

$$\mathbb{M}_{ij}^{\text{new}} = \mathbb{M}_{ij} - u_k (\partial_k \mathbb{M}_{ij}) + (\partial_k u_i) \mathbb{M}_{kj} + \mathbb{M}_{ik} (\partial_k u_j), \quad (3)$$

ensuring the confluence of the tissue. Additionally, a free energy density can be written in terms of \mathbb{M} , as

$$f(\mathbb{M}) = \frac{1}{c_1 \sqrt{\det \mathbb{M}}} \left\{ \frac{K_A}{2} (c_1 \sqrt{\det \mathbb{M}} - A_0)^2 + \frac{K_P}{2} \left[c_2 \sqrt{\text{tr} \mathbb{M}} - \left(P_0 - \frac{J}{2K_P} \right) \right]^2 \right\} \quad (4)$$

such that the total elastic energy (1) is obtained as $E = \int f(\mathbb{M}(\mathbf{r})) d^2r$, with the areas and perimeters obtained from \mathbb{M} , as in Ref.¹² (see App. A for details). See Refs.²³ and²⁴ for other similar 2×2 symmetric tensors used to describe cell shapes in continuum models of tissues.

Since the tensor field $\mathbb{M}(\mathbf{r})$ is symmetric, it can be represented as $\mathbb{M} = M e^{c\Theta(\theta)}$, where M , c and θ are scalar fields. M represents the coarse-grained cellular area (over c_1); c , the coarse-grained cell shape anisotropy; and θ , the coarse-grained cell orientation, in term of which the trace-less tensor Θ is given by

$$\Theta = \begin{pmatrix} \cos 2\theta & \sin 2\theta \\ \sin 2\theta & -\cos 2\theta \end{pmatrix}. \quad (5)$$

In this representation, $c = \ln(s_1/s_2)$, where s_1 and s_2 are the semi-axis of the approximated ellipse-shape, with s_1 oriented along θ . Then, $c > 0$ ($c < 0$) represents cellular elongation (contraction) in the direction defined by θ .

With the previous representation of \mathbb{M} , its determinant and trace are given by $\det \mathbb{M} = M^2$ and $\text{tr} \mathbb{M} = 2M \cosh(c)$. Following the procedure shown in Ref.¹² using Eq. 3, it is possible to derive the associated elastic stress tensor given by a combination of an isotropic pressure and a deviatoric tensor, related to the tension at the cellular junctions: $\sigma_e = -p_e \mathbb{1} + \sigma_{e,\text{dev}}$ (App. A), with

$$p_e = -K_A (c_1 M - A_0) - K_P \frac{c_2}{c_1} \left[c_2 - \frac{P_0 - J/(2K_P)}{\sqrt{2M \cosh(c)}} \right] \cosh(c), \quad (6)$$

$$\sigma_{e,\text{dev}} = K_P \frac{c_2}{c_1} \left[c_2 - \frac{P_0 - J/(2K_P)}{\sqrt{2M \cosh(c)}} \right] \sinh(c) \Theta. \quad (7)$$

We recall that the areas and perimeters are correctly computed in terms of \mathbb{M} up to order ε in the deformations. Therefore, as Eqs. (6) and (7) linearly depend on the areas and perimeters, the stresses are correct also to linear order in the deformations.

3 Inhomogeneous activity

In Ref.¹² they use a similar form of the previous stress tensor. In all their applications (externally induced axial stretch, deformation due to active internal forces, and generation of shear flow) they assume for simplicity that \mathbb{M} is homogeneous, and the field M is constant. Here, we consider the case of epithelial tissues performing inhomogeneous apical contractions, resulting in texture

and stress tensors that are inhomogeneous.

In many circumstances, epithelial tissues exhibit dramatic alterations at the apical cellular surface. Particularly, the contraction of the apical face (reviewed in Ref.²⁵) is a fundamental mechanism of tissue remodeling. Apical contractions are seen during localized processes such as cell divisions or extrusions²⁶, as well as during major coordinated cell movements such as ventral furrow formation in *Drosophila*²⁷, or the stage preceding epiboly in *Austrolebias nigripinnis*²⁸. In a previous article¹¹, we addressed and computationally modeled the apical contraction of a single cell embedded in a tissue described with the vertex model, as an active process related to internal changes at specific cellular regions, medial and periphery. Similarly, other researchers have explored the mechanical responses in tubular epithelial systems²⁹ using the premise that all cells are actively contracting. They observed that cell-level geometrical changes generated by belt-like and mesh-like activities influence tube-level stiffness. On the other hand, Spahn *et al.*¹³ specifically analyzed the ventral furrow formation in *Drosophila*, taking into account active energy terms proportional to cell areas and junction lengths to generate the apical contractions, and were able to predict the experimentally observed anisotropic constriction.

The microscopic description of the vertex model (at the level of individual cells and vertices) can be too detailed when describing large tissues, making it hard to make analytical progress. Furthermore, for tissues that present some spatial symmetries, it is not direct to theoretically impose those symmetries on the vertex displacements. It is, then, natural to apply the continuum description for the analysis of inhomogeneous apical contractions.

In the vertex model, medial and perimeter activities associated to apical contractions are represented by inhomogeneous modifications of the target quantities, as $A_0 \rightarrow A_0 + \Delta_A(\mathbf{r})$ and $P_0 \rightarrow P_0 + \Delta_P(\mathbf{r})$. Since the shape index here is given by $p_0 = [P_0 - J/(2K_P)]/\sqrt{A_0}$, these inhomogeneous activities induce inhomogeneities in p_0 , which is known to control fluidity in the classical vertex model³⁰, and its heterogeneity has been proven to enhance rigidity⁷. Using Eqs. (6) and (7), the stresses associated with the activities are given by $\sigma_{A_0} = -p_{A_0}\mathbb{1}$ and $\sigma_{P_0} = -p_{P_0}\mathbb{1} + \sigma_{P_0,\text{dev}}$, with

$$p_{A_0} = \Delta_A K_A, \quad (8)$$

$$p_{P_0} = \frac{\Delta_P}{\sqrt{2M}} K_P \frac{c_2}{c_1} \sqrt{\cosh(c)}, \quad (9)$$

$$\sigma_{P_0,\text{dev}} = -\frac{\Delta_P}{\sqrt{2M}} K_P \frac{c_2}{c_1} \frac{\sinh(c)}{\sqrt{\cosh(c)}} \Theta. \quad (10)$$

While medial activity generates a pressure field p_{A_0} (explicitly) independent of cell size (M) and shape (c), perimeter activity generates a pressure p_{P_0} and a deviatoric stress $\sigma_{P_0,\text{dev}}$, both of them with inverse relation with size ($\sim 1/\sqrt{M}$), and dependent on shape. Both active pressures take the sign of the active term $\Delta_{A,P}$. Instead, the sign of the active deviatoric stress $\sigma_{P_0,\text{dev}}$ depends on both Δ_P and c . Then, negative $\Delta_{A,P}$ generates negative active pressures, causing cellular compression and local shape vari-

ations. Additionally, junctions will actively change their tension in the case of perimeter activity, depending on shape (elongation/contraction) and orientation. For example, for an initially isotropic tissue ($\theta = 0$) under a negative activity that only depends on the horizontal position $\Delta_P = \Delta_P(x) < 0$, elongated (contracted) junctions oriented in $\hat{\mathbf{x}}$ will actively increase (decrease) their tension, increasing shape isotropy, as shown at the single-cell activity level in Ref.¹¹. The latter implies that $\Delta_P < 0$ locally solidifies the tissue, as expected in a system locally decreasing p_0 .

The tissue's steady-state under these inhomogeneous activities is obtained imposing the force balance, $\nabla \cdot \sigma = 0$, i.e.,

$$\nabla \cdot (p_e + p_{A_0} + p_{P_0}) = \nabla \cdot (\sigma_{e,\text{dev}} + \sigma_{P_0,\text{dev}}). \quad (11)$$

To analyze the temporal evolution, we make an analogy to the equation of motion for an isotropic elastic medium³¹. We equate the internal force coming from the total stress tensor $\nabla \cdot \sigma$, to the product of the velocity times the friction per unit area of the body (the vertex), i.e., $\tilde{\mu} = \mu/A_v$, where A_v is the mean area occupied by a vertex. The resulting dynamical equation is then given by

$$\frac{\mu}{A_v} \frac{\partial \mathbf{u}(\mathbf{r}, t)}{\partial t} = \nabla \cdot [\sigma_e(\mathbf{r}, t) + \sigma_{A_0}(\mathbf{r}, t) + \sigma_{P_0}(\mathbf{r}, t)]. \quad (12)$$

To summarize, the static and dynamic continuum descriptions are for the displacement field \mathbf{u} , obeying the mechanical equations (11) and (12) in terms of the stress tensor, which is computed from the texture field using equations (6) and (7). Finally, the texture field satisfies the confluence condition (3) in terms of the displacement field, closing the system of equations. Activity provides additional stresses, Eqs. (8)-(10), driving the tissue to new configurations.

4 Application: Simple active stripe

To keep it simple but biophysically relevant, we apply the previous continuum description to the case of a stripe patch with a negative activity, which varies with a Gaussian profile inside the stripe, and compare results with numerical simulations using the vertex model (microscopic description). This kind of activity causes cellular contractions as experimentally seen during the ventral furrow formation in *Drosophila*^{13,27}. The case of a circular active patch, which produces apical geometries as seen in cyst formation³² and is more exigent to the theory, is analyzed App. C.

Both for the vertex model and continuum descriptions, we set units by choosing $A_0 = \langle A_{0c} \rangle = 1$, $K_A = 1$, and $\mu = 1$, and define the dimensionless parameters $\hat{K}_P = K_P/(K_A A_0)$ and $\hat{J} = J/(K_A A_0^{3/2})$.

To obtain a mechanically stable tissue³³ where no T1 events will be required in the numerical simulations, we chose the values $\hat{K}_P = \hat{J} = 1$.

For the microscopic description, first we consider an initial two-dimensional ordered tissue made up of identical regular hexagonal cells, with uniform $A_{0c} = 1$ and $P_{0c} = 3.72$, and then an isotropic disordered confluent tissue with non-uniform preferred quantities A_{0c} and P_{0c} . To create the disordered tissue we built Voronoi cells where 3000 center points are generated by a Monte Carlo simulation of hard disks in a box of dimensions $L_x \times L_y$ (Table 1), with periodic boundary conditions. The diameter of the

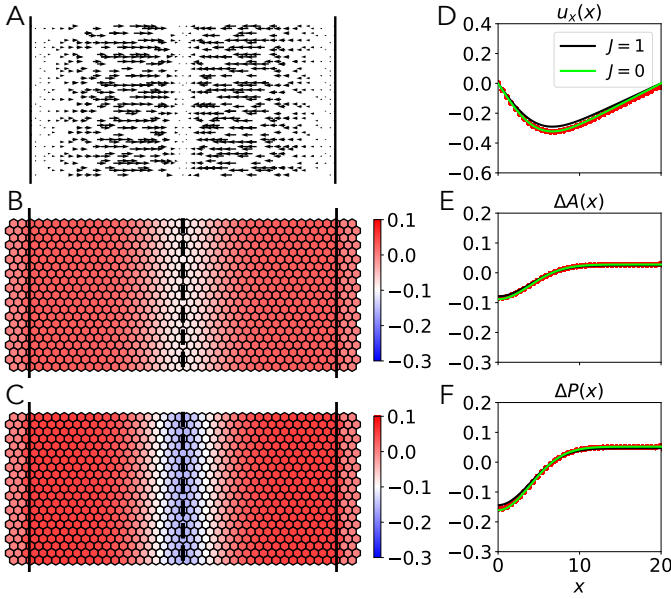


Fig. 1 Contraction of a simple active stripe for regular hexagonal cells. Results of the simulated epithelial tissue made of initially regular hexagonal cells of area equals one, with $K_A = 1$, $K_P = 1$, $A_0 = 1$, $P_0 = 3.72$, and $J = 1$, under medial activity ($\lambda_A = 0.5$, $\lambda_P = 0$, $R = 3$, and $W_{\text{half-box}} = 14$) at $t = 100$, versus the initial position of the vertex or cell centers. (A) Vectorial map of the total vertex displacement in a representative tissue section, in units of $\sqrt{A_0}/5$. (B) Representative section of the tissue, showing area change. (C) Representative section of the tissue, showing perimeter change. (D) Scatter plot of the horizontal displacement of vertices (red dots). (E) Scatter plot of the area change (red dots). (F) Scatter plot of the perimeter change (red dots). In A-B-C the solid-black curves represent the distance $x = \pm W_{\text{half-box}}$. In D-E-F, the x axis gives the initial position of the vertices or cell centers and the solid-black (lime) curves show the outcomes of the continuum description, with $J = 1$ ($J = 0$), $A_0 = 1$, $P_0 = 3.72$, $c_1 = 3\sqrt{3}/2$, and $c_2 = 3\sqrt{2}$.

disks govern the degree of dispersion of the cells. We consider an area fraction $\phi = 0.71$ ³³, below the freezing transition, obtaining polygons with areas and perimeter that define A_{0c} and P_{0c} for each cell, with $\langle A_{0c} \rangle = 1$ and $\langle P_{0c} \rangle = 3.9$ (see App. B for more details). Particularly, we begin with a solid-tissue arrangement with mean shape index $\langle p_{0c} \rangle = 3.4$. The system is then allowed to relax using the parameters shown in Table 1, in the absence of activity. The relaxed state defines the initial configuration of our entire tissue, and has polygonal shapes from squares to nonagons, with mean area $\langle A_c \rangle = 1$ and mean perimeter $\langle P_c \rangle = 3.77$ (App. B). Note that the value of $\langle A_c \rangle$ is preserved during relaxation because the tissue is confluent, and hence the total area does not change.

The active stripe is built as follows. We define an active axis along the y direction, with a random x position and we clamp all vertices that are further than $W_{\text{half-box}} = 20$ away from this active axis (i.e., we impose no motion on these vertices). Then, we end up working with a smaller tissue made up of ~ 2200 cells that has periodic boundary conditions on the y -axis, and fixed boundary conditions on the x -axis. Medial and perimeter activities are included as $\Delta A = -\lambda_A A_{0c} \Gamma(x)$ and $\Delta P = -\lambda_P P_{0c} \Gamma(x)$, with $\Gamma(x) = \exp(-x^2/2R^2)$, and R indicating the active region extension. These changes cause spatial-dependent cellular contractions, as seen in Fig. 2. More specifically, the addition of medial

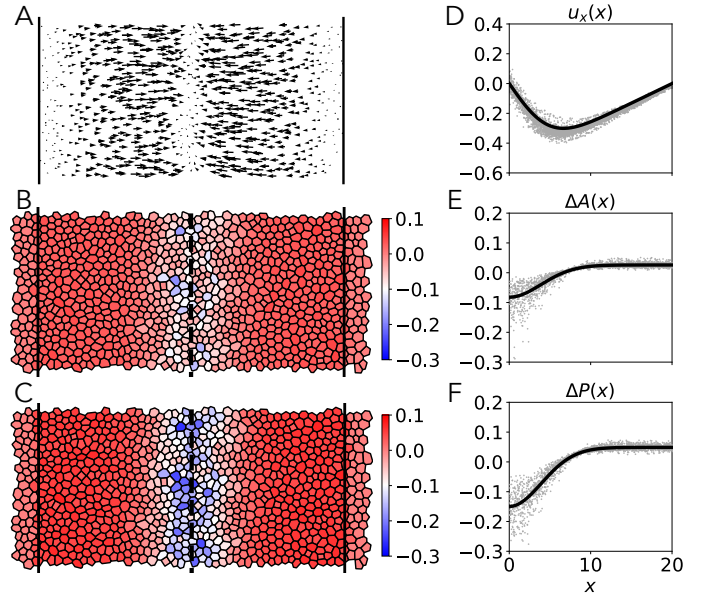


Fig. 2 Contraction of a simple active stripe for a disordered tissue. Results of a simulated epithelial tissue with medial activity ($\lambda_A = 0.5$, $\lambda_P = 0$, $R = 4$, $W_{\text{half-box}} = 20$) at $t = 100$. (A) Vectorial map of the total vertex displacement in a representative tissue section, in units of $[\sqrt{A_0}/5]$. (B) Area change in a representative section of the tissue. (C) Perimeter change in a representative section of the tissue. (D) Scatter plot of the horizontal displacement of each vertex. (E) Scatter plot of the area change. (F) Scatter plot of the perimeter change. The dashed line in B-C shows the active axis ($x = 0$). In A-B-C the solid-black curves represent the distance $x = \pm W_{\text{half-box}}$. In D-E-F, the x axis gives the initial position of the vertices or cell centers, and the solid-black curves show the outcomes of the continuum description.

(perimeter) activity locally raises (decreases) p_{0c} , to values that depend on the distance to the active axis. Finally, we let the system evolve by integrating the dynamical equation for \mathbf{r}_i , using the Euler method with $dt = 0.05$, up to $t = 100$, reaching a steady-state.

4.1 Steady state

We analyze the final (steady) state of the simple active stripe simulations by quantifying the displacement of the vertices and the area and perimeter changes of the cells. Figs. 1 (ordered tissue) and 2 (disordered tissue) show these three quantities for an active patch defined by $R = 4$, under medial activity ($\lambda_A = 0.5$, $\lambda_P = 0$), with $x = 0$ the position of the active axis (dashed-black lines), and x the distance (in absolute value) from it. Figs. 1A (ordered tissue) and 2A (disordered tissue) show the vectorial map of \mathbf{u} , with horizontal and vertical components. For clarity, only the vector of one vertex per cell is shown. Small magnitudes of \mathbf{u} (black arrows in units of $[\sqrt{A_0}/5]$) are obtained with the active parameters considered in this work, and then cells conserve their neighbors all the time. Initial geometrical disorder enhances local vertical components in the displacement, with positive and negative signs in different regions. However, in both tissues we obtain a horizontal net displacement when taking the average response of the vertices. Figs. 1B-C (ordered tissue) and 2B-C (disordered tissue) show the color map of the obtained area changes ΔA , and

perimeter changes ΔP , respectively. ΔA decreases near the active axis and increases away from it due to total area conservation. ΔP has the same qualitative behavior.

We proceed to analyze the steady state using the continuum description. For that, we consider an initial isotropic tissue with uniform \mathbb{M} , defined by $M(t=0) = m = A_0/c_1, c(t=0) = 0$ and $\theta(t=0) = 0$. Since the activities depend on the horizontal position only, we use that spatial symmetry to impose that $\mathbf{u} = u_x(x)\hat{\mathbf{x}}$, and $\theta(x) = 0$ (contractions and elongations along the x -axis). Then, the confluence condition for the tissue [Eq. (3)] reads

$$M \begin{pmatrix} e^c & 0 \\ 0 & e^{-c} \end{pmatrix} = m \begin{pmatrix} 1 + 2 \frac{du_x}{dx} & 0 \\ 0 & 1 \end{pmatrix}, \quad (13)$$

representing a functional relation between the scalar fields M and c , and the displacement field $u_x(x)$, from where we obtain

$$M(x) = m \sqrt{1 + 2 \frac{du_x}{dx}}, \quad (14)$$

$$\cosh[c(x)] = \frac{m}{M(x)} \left(1 + \frac{du_x}{dx} \right) = \frac{1 + \frac{du_x}{dx}}{\sqrt{1 + 2 \frac{du_x}{dx}}}, \quad (15)$$

$$\sinh[c(x)] = \frac{m}{M(x)} \frac{du_x}{dx} = \frac{\frac{du_x}{dx}}{\sqrt{1 + 2 \frac{du_x}{dx}}}, \quad (16)$$

and then $e^c = \cosh[c(x)] + \sinh[c(x)] = \sqrt{1 + 2 \frac{du_x}{dx}}$.

The steady-state condition [Eq. (11)] in this case is given by

$$0 = \frac{\partial \sigma_e^{xx}}{\partial x} + \lambda_A K_A A_0 \frac{\partial \Gamma(x)}{\partial x} + \lambda_P P_0 K_P \frac{c_2}{c_1} \frac{\partial}{\partial x} \left[\frac{e^c \Gamma(x)}{\sqrt{2M \cosh(c)}} \right], \quad (17)$$

where

$$\sigma_e^{xx} = K_A (c_1 M - A_0) + K_P \frac{c_2}{c_1} \left(c_2 - \frac{P_0 - J/(2K_P)}{\sqrt{2M \cosh(c)}} \right) e^c. \quad (18)$$

Finally, we can write each term in Eq. (17) in terms of x , $u_x(x)$, $u'_x(x)$, and $u''_x(x)$, obtaining an ordinary differential equation which we numerically solve imposing $u_x(x=0) = 0$, $u_x(x = W_{\text{half-box}}) = 0$.

First, we compare the results from numerical simulation using the ordered tissue with the ones obtained from the continuum description when considering $A_0 = 1$, $P_0 = 3.72$, $c_1 = 3\sqrt{3}/2$, and $c_2 = 3\sqrt{2}$ (hexagon values). As a result, we obtain $u_x(x)$ and use it to compute ΔA and ΔP . Due to the symmetry of the regular hexagonal lattice, and the borders of the tissue being clamped, no net effect of J over the tissue dynamics is expected. Indeed, we obtained that the results from the numerical simulations are independent of J , and hence saying $J = 1$ is the same as $J = 0$, for the ordered tissue. However, we find that the solution of our continuum description changes when varying J as seen in Fig. 1D-E-F (black and lime curves). Figs. 8 and 12 show the same result, under different lattices and symmetries. This is an effect of approximating areas and perimeters as being simply proportional to $\sqrt{\det \mathbb{M}}$ and $\sqrt{\text{tr} \mathbb{M}}$, respectively. Then, more complex expressions for the area and perimeter would be needed in order to recreate

the tissue dynamical independence of J in ordered tissues. Nevertheless, we will show that under our simple definitions, with shape being defined by only two degrees of freedom (fields M and c), we can very closely describe disordered tissues.

For the disordered tissue used in numerical simulations, since it is isotropic and has a majority of hexagons (Fig. 7), we keep the values $c_1 = 3\sqrt{3}/2$ and $c_2 = 3\sqrt{2}$, and consider initial areas and perimeters given by a hexagonal lattice ($A_{\text{hex}} = 1$, $P_{\text{hex}} = 3.72$). Figs. 2D-E-F show the results obtained by the continuum description (solid-black curves), together with ΔA and ΔP measured in the vertex model simulations using the disordered tissue. App. C presents the case of an active circular region of Gaussian size $R = 4$, for the ordered and disordered tissue.

As seen in Fig. 2, vertex model simulations using the disordered tissue show important fluctuations in the different observables. To quantify this, Fig. 3 shows the probability density function by column, of u_x , ΔA , and ΔP , for the cases of medial and perimeter activity, considering 100 different simulations (random active axis positions) for each case. Again, solid-black curves show the results obtained from solving the steady-state condition. In both descriptions, i) the maximum area and perimeter change ($\Delta A_{\text{max}}, \Delta P_{\text{max}}$) is reached at the active axis ($x = 0$); ii) the area change changes its sign due to the total area conservation, defining a region under contraction and another under expansion; iii) the displacement has a well-defined minimum (maximum displacement, u_{max}). Additionally, the geometrical response under medial activity presents more variability than under perimeter activity (Fig. 3).

To quantitatively test our agreement between the discrete (vertex model) and the continuum description, we analyze three experimentally interesting and measurable observables for different active patch sizes R . i) maximum contraction (ΔA_{max}), ii) maximum horizontal displacement (u_{max}), and iii) the position at which the displacement is maximum ($x_{\text{max},d}$). In Fig. 4, we compare the observables in the final steady state, under medial ($\lambda_A = 0.5$) and perimeter ($\lambda_P = 0.1$) activity, finding an excellent agreement even for small values of R ($R \sim \text{cell size}$). We consider different intensities for the activities, with $\lambda_A > \lambda_P$, because the ratio between the active forces goes like $f_{A_0}/f_{P_0} \sim \lambda_A / [\lambda_P (K_P / (K_A A_0)) (P_0 / \sqrt{A_0}) (c_2 / \sqrt{c_1})]$, and since $K_P / (K_A A_0) = 1$, $P_0 / \sqrt{A_0} = 3.9$, and $c_2 / \sqrt{c_1} = 2.63$ for the hexagonal case, $f_{A_0}/f_{P_0} \sim \lambda_A / (10\lambda_P)$. As a result of the areas and perimeter approximations, the continuum description slightly under predicts the maximum contraction and horizontal displacement (black lines above mean values in Fig. 4A-B). Nevertheless, the results for the maximum contraction obtained from the continuum description lie inside the error bars of the discrete simulations. Consistent with Fig. 3, the change in area presents larger fluctuations for medial activity compared to activity in the perimeter. Interestingly, the standard deviations of the maximum horizontal displacement u_{max} and the values of $x_{\text{max},d}$, are remarkably similar for both activities. The cases of an active circular region (App. C) and a tissue made of square cells (App. D) present similar results.

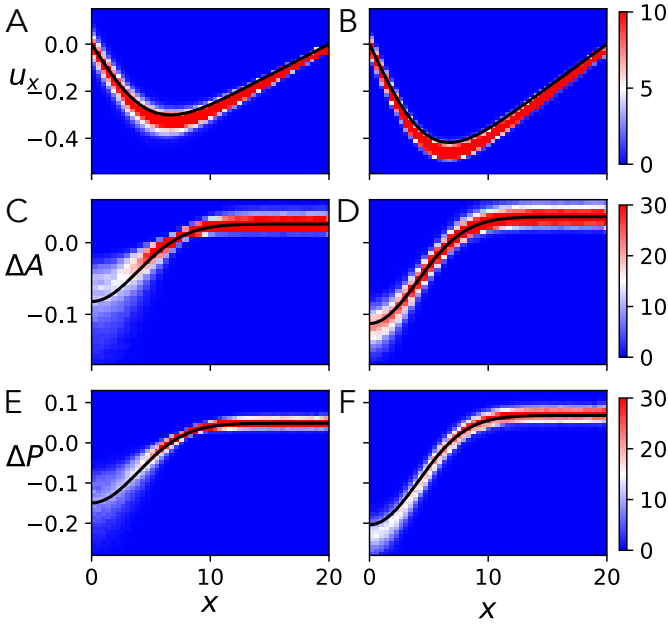


Fig. 3 Statistical analysis of the tissue-level response on the simple active stripe. Probability density function by column, obtained from 100 simulations with randomly chosen active axis, at $t = 100$, versus the initial position of the vertex or cell center. Left: simple active stripe with medial activity ($\lambda_A = 0.5, \lambda_P = 0, R = 4$). Right: simple active stripe with perimeter activity ($\lambda_A = 0, \lambda_P = 0.1, R = 4$). (A)-(B) Horizontal displacements of the vertices. (C)-(D) Cellular area change ΔA . (E)-(F) Cellular perimeter change ΔP . The solid-black curves show the outcomes of the continuum description.

4.2 Temporal evolution

We numerically solve Eq. (12) imposing $u_x(x, t = 0) = 0$, $u_x(x = 0, t) = 0$, and $u_x(x = W_{\text{half-box}}, t) = 0$. Since the original tissue obeys periodic boundary conditions, Euler's characteristic formula is given by $V - E + C = 0$ (V : vertices, E : edges, C : cells). Additionally, in our tissue, vertices are formed by the intersection of three junctions, and then the coordination number is $2E/V = 3$. By using both equations, we obtain the ratio $C : V = 1 : 2$, and then the area occupied by each vertex that appears in Eq. (12) is $A_v = 1/2$, in units of A_0 .

We compare the temporal evolution of the observables between both descriptions in Fig. 5, finding an excellent agreement. For both activities, $\sigma_{u_{\max}}$ is small and very similar, showing independence with respect to the sign of the change (increase/decrease) of shape index p_0 . Instead, $\sigma_{\Delta A_{\max}}$ does depend on p_0 , and is larger for medial activity, i.e., tissues with a core that has been actively fluidized (increased p_0). The numerical simulations using a disordered tissue allow us to obtain the dynamic evolution of each observable variance, paving the road for a theory beyond the mean field that depends on the tissue fluidity. For the temporal evolution of the disordered tissue under a circular active region, and the tissue made of square cells under a simple active stripe, see App. C and App. D, respectively.

The non-uniform distributions of A_{0c} and P_{0c} in the numerical simulations add an extra source of mechanical heterogeneity. We measure the rate of change of the area of cells whose centers are initially at less than $R/2$ from the active axis. For these cells

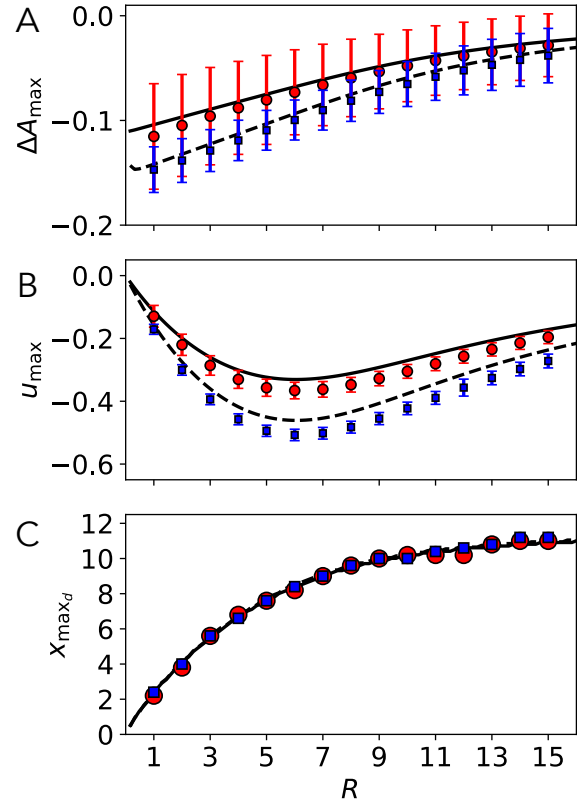


Fig. 4 Comparison of micro and macro descriptions of the steady-state. (A) Maximum contraction for different active stripe sizes R . (B) Maximum horizontal displacement. (C) Position at which the horizontal displacement is maximum. Black curves show the outcomes of the continuum description, for medial ($\lambda_A = 0.5, \lambda_P = 0$) (solid-line) and perimeter ($\lambda_A = 0, \lambda_P = 0.1$) (dashed-line) activity. Red circles and blue squares represent the numerical results averaged over 100 simulations with different active axes for each integer R from 1 to 15. Bars show the standard deviations of ΔA and u at the position of maximum contraction and displacement, respectively.

$\Gamma(x) \in [0.88, 1]$ is rather homogeneous, and then heterogeneity in activity comes mainly from the differences in A_{0c}, P_{0c} . The cell growth rates show two different regimes, namely for early times ($t = 0.1$) and late times ($t = 1$). Fig. 6 shows these area rates for the case for medial activity ($\lambda_A = 0.5, \lambda_P = 0, R = 4$, same simulation shown in Fig. 2), and perimeter activity ($\lambda_A = 0, \lambda_P = 0.1, R = 4$). At early times, for both activities, we find that some cells grow, while other shrink. For late times, all the cells are shrinking. Additionally, the distribution of growing/shrinking cells at short times depends on the kind of activity. For medial activity, big cells, which happen to have high sidedness (≥ 6), contract first, with a rate that increases with the cell size, Fig. 6A. For perimeter activity, cells with low sidedness (≤ 6) contract first. However, inside each family of polygons the contraction rate increases with size as in the medial activity case, creating the clustering in lines observed in Fig. 6B. The continuum description of the tissue is consistent with these results. Indeed, in the continuum formulation, the contraction rate is proportional to the rate of deformation, which has a global size dependence (as seen in Eq. (12)), as well as specific dependences originating from the

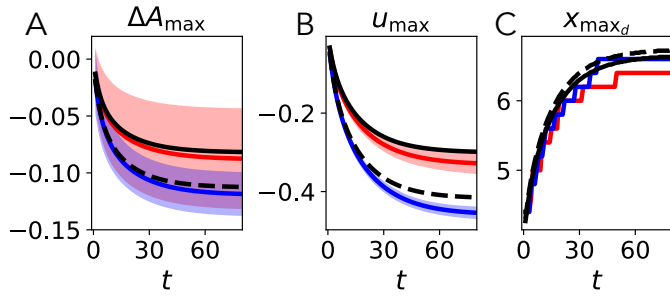


Fig. 5 Comparison of micro and macro descriptions of the tissue evolution in time. (A) Maximum contraction in time. (B) Maximum horizontal displacement. (C) Position at which the horizontal displacement is maximum. Black curves show the outcomes of the continuum description, for medial ($\lambda_A = 0.5, \lambda_P = 0, R = 4$) (solid-line) and perimeter ($\lambda_A = 0, \lambda_P = 0.1, R = 4$) (dashed-line) activity, with $\bar{\mu} = 2\mu$. Solid-red and solid-blue curves represent the numerical mean results obtained from 100 simulations with a different active axis. Shaded areas represent standard deviations of ΔA and u at the position of maximum contraction and displacement, respectively.

different forces. Specifically, the active forces (second and third terms in Eq. (17)) have the pre-factors A_0 for the medial case and $P_0(c_2/c_1)$ for the perimeter case. We find that in our isotropic disordered tissue A_{0c} and P_{0c} increase with cell size in the initial configuration (Fig. 7C-D), whereas the term (c_2/c_1) decreases with the number of sides of a given polygon Fig. 7B. Since our tissue is initially isotropic ($c(t=0) \approx 0$ for all cells), we see from Eqs. (9) and (10) that perimeter active pressure initially dominates over the perimeter active tensions, causing cellular contraction and shape deformations, changing c and hence increasing active tensions. Since $\sqrt{\cosh c}$ is an even function and $\sinh c$ is an odd function, $\sigma_{P_0,dev}$ increases if elongated ($c > 0$), and decreases if contracted ($c < 0$). Then, the active tension regulates forces in order to increase isotropy.

5 Conclusions

We developed a continuum model for confluent epithelial tissues under spatial inhomogeneous cellular activity, constructed from the stress tensor of the cell-level vertex model. Here, activity directly changes the target cell shape index p_0 , which has been shown to control fluidity in homogeneous tissues³⁰. Our continuum model shows that active changes in the target cell shape index are directly linked to cellular stresses. Activity in the medial region of the cell generates an isotropic pressure (explicitly) independent of shape, while activity in the perimeter region of the cell generates an isotropic pressure and a deviatoric (traceless) stress, both of them with an explicit dependence on shape and size. Particularly, the active deviatoric stress acts against the shape anisotropy and vanishes under isotropic configurations.

To test the validity of the continuum description, we compared the steady-state and time-dependent solutions with computer simulations of isotropic disordered tissues using the vertex model. We used inhomogeneous target areas and perimeters to represent inhomogeneous patches presenting apical contractions. Particularly, we analyzed the case of a simple active stripe, where activity decreases with distance from an active axis, proportional

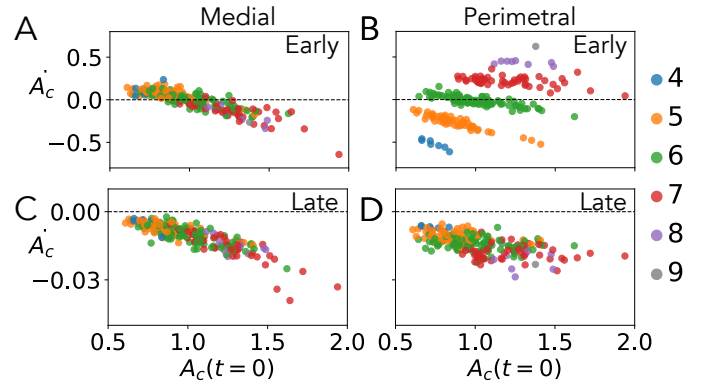


Fig. 6 Cell-level growth rate. Left: simple active stripe with medial activity ($\lambda_A = 0.5, \lambda_P = 0, R = 4$). The same simulation is used in Fig. 2. Right: simple active stripe with perimeter activity ($\lambda_A = 0, \lambda_P = 0.1, R = 4$). We consider the 221 cells whose centers are initially at a distance smaller than $R/2$ from the active axis. The rate for each cell is defined as $\dot{A}_c = [A_c(t+\Delta) - A_c(t)]/\Delta$, with $\Delta = 0.1$. (A)-(B) Scatter plot of the 221 rates versus the initial cell area $A_c(t=0)$, at $t = 0.1$. (C)-(D) Scatter plot of the 221 rates versus the initial cell area $A_c(t=0)$, at $t = 1$. The colors indicate the number of sides of each cell.

to a Gaussian function. Remarkably, our continuum formulation that uses only two degrees of freedom to define shape, presents excellent agreement when using the exact cell-level parameters of the vertex model simulations. Similar results are reported when considering a circular active region (App. C) and a simple active stripe over a tissue made of square cells (App. D).

T1 topological events, which drive relative cellular motion, were unnecessary here since the levels of activity used in this work generate small deformations. Then, all tissues considered in this work are in a solid state by definition. Nevertheless, numerical simulations show that different levels of geometrical variation arise as a non-dynamic quantification of how cellular activity affects tissue fluidity. As a liquid versus solid behavior, medial activity (increasing p_0) produces more significant cell-level geometrical variations than perimeter activity (decreasing p_0). Interestingly, no significant difference is seen at the vertex level.

Additionally, we found that heterogeneous preferred areas and perimeters in the vertex model induce mechanical heterogeneity even when the active functions are mostly uniform. In particular, we measured the rate of cell contraction/expansion at short times for cells close to the active axis. Since our tissues are initially isotropic, active pressures dominate. The active force under medial activity depends on the size only, and particularly bigger cells contract first. Instead, under perimeter activity, the active force inducing contraction depends on both polygon size and sidedness. We find that cells with lower sidedness contract first, while maintaining the positive correlation between cell size and rate of contraction. In the second case, cellular contraction in a confluent system leads to shape changes, turning on the active tensions that increase isotropy in the system. The latter is related to experimental observations and computational models, showing that more compact cells tend to be more solid (lower p_0), whereas elongated cells increase the tissue fluidity (larger p_0)^{30,34-36}.

Further research directions include examining the fluid/solid

dynamic disparities caused by inhomogeneous cellular activity, spatial and temporal, in motile tissue models and analyzing the cell level shape dynamic in anisotropic pre-stressed tissues. Also, rules for cellular division and extrusion could be considered, as in Ref.²⁰, where they can explain different extrusion rates caused by similar activities.

A Elastic stress tensor derivation

To obtain an elastic stress that depends on geometrical shapes, we use the texture matrix [Eq. (2)]. Then, the area and perimeter of the cell can be written as $A_c = c_1 \sqrt{\det \mathbb{M}_c}$ and $P_c = c_2 \sqrt{\text{tr} \mathbb{M}_c}$, respectively, with c_1 and c_2 depending on the type of polygon. Hence, the energy functional [Eq. (1)] for a tissue with periodic boundary conditions turns to be equal to

$$E = \frac{K_A}{2} \sum_c \left(c_1 \sqrt{\det \mathbb{M}_c} - A_{0c} \right)^2 + \frac{K_P}{2} \sum_c \left[c_2 \sqrt{\text{tr} \mathbb{M}_c} - \left(P_{0c} - \frac{J}{2K_P} \right) \right]^2. \quad (19)$$

We perform a coarse-graining over the discrete perspective of the tissue to obtain a smooth symmetric tensor field $\mathbb{M}(\mathbf{r})$, which represents the shape at a tissue scale. We define the energy density per unit area [Eq. (4)], such that the total elastic energy is $E = \int f(\mathbb{M}(\mathbf{r})) d^2r$, as in Ref.¹². Analogous to Ref.¹², we compute the elastic stress as $\sigma_e = f \mathbb{1} + 2(\partial f / \partial \mathbb{M}) \mathbb{M}$. Using that $\partial \text{tr} \mathbb{M} / \partial \mathbb{M} = \mathbb{1}$ and $\partial \det \mathbb{M} / \partial \mathbb{M} = (\det \mathbb{M}) \mathbb{M}^{-1}$, the elastic stress tensor is finally given by

$$\begin{aligned} \sigma_e &= K_A \left(c_1 \sqrt{\det \mathbb{M}} - A_0 \right) \mathbb{1} \\ &+ \frac{c_2 K_P}{c_1 \sqrt{\det \mathbb{M}} \sqrt{\text{tr} \mathbb{M}}} \left[c_2 \sqrt{\text{tr} \mathbb{M}} - \left(P_0 - \frac{J}{2K_P} \right) \right] \mathbb{M}, \\ &= K_A (c_1 M - A_0) \mathbb{1} + K_P \frac{c_2}{c_1} \left(c_2 - \frac{P_0 - J/(2K_P)}{\sqrt{2M \cosh(c)}} \right) \frac{\mathbb{M}}{M}, \end{aligned} \quad (20)$$

where we used that for $\mathbb{M} = M e^{c\Theta}$, $\det \mathbb{M} = M^2$ and $\text{tr} \mathbb{M} = 2M \cosh(c)$. Since $\mathbb{M} = M e^{c\Theta} = M \cosh(c) \mathbb{1} + M \sinh(c) \Theta$, we can rewrite the last term in Eq. (20), identifying the pressure [Eq. (6)] and a deviatoric (trace-less) elastic stress [Eq. (7)].

B Simulations details

The initial (relaxed) configuration of our entire disordered tissue in the numerical simulations, has polygonal cellular shapes from squares to nonagons, with majority of hexagons, and $\langle A_c \rangle = 1$ and $\langle P_c \rangle = 3.77$ (Fig. 7).

For the case of the active stripe in the disordered tissue, for each simulation we randomly choose a cell whose horizontal position defines the position of the active axis. Then, through the simulations we keep fixed all the vertices that belong to cells whose centers lie further away than $W_{\text{half-box}} = 20$, from the active axis. In each simulation with an active stripe, the effective tissue has ~ 2200 cells, vertical periodic boundary conditions, and horizontal fixed boundary conditions.

For the case of the circular active patch in the disordered tissue, for each simulation we randomly choose a cell whose center defines the origin of activity. Then, through the simulations we keep

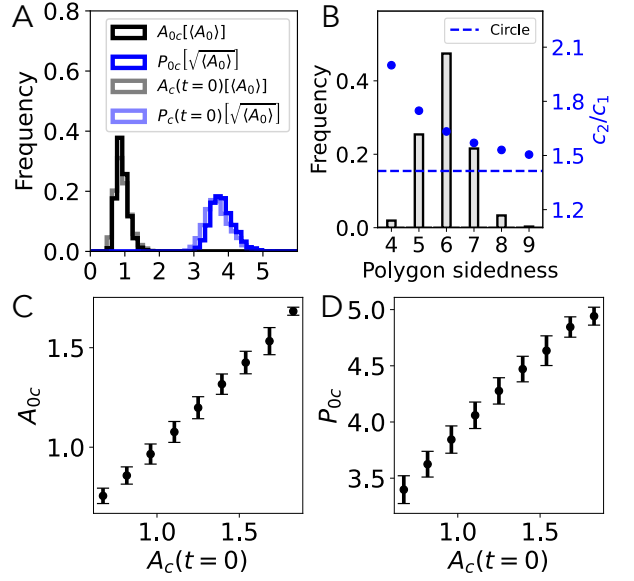


Fig. 7 Initial configuration of the relaxed disordered tissue. (A) Histograms of the cell target area, target perimeter, initial area, and initial perimeter. $\langle A_{0c} \rangle = \langle A_c \rangle = 1$, $\langle P_{0c} \rangle = 3.9$, $\langle P_c \rangle = 3.77$. (B) Histogram of polygon sidedness in gray bars. Ratio c_2/c_1 as a function of polygon sidedness, for regular polygons (blue dots). The dashed line represents the value for a circle (limit of an infinite number of sides). (C) Correlation between target area and initial area. (D) Correlation between target perimeter and initial area. Error bars represent ± 1 standard deviation.

fixed all the vertices that belong to cells whose centers lie further away than $W_{\text{half-box}} = 24$ from the active origin. In each simulation with a circular active patch, the effective tissue has ~ 1800 cells, and fixed boundary conditions.

Every simulation is run using the parameters from Table 1, with $W_{\text{half-box}} = \{20, 24, 14\}$ for the disordered and regular tissue with a simple active stripe, for the disordered and regular tissues with a circular active patch, and for the tissue made of square cells with a simple active stripe, respectively.

Table 1 Simulations parameters

Parameter	Symbol	Value
Area elastic modulus	K_A	1
Perimeter elastic modulus	K_P	1
Constant line tension	J	1
Mean target area	$A_0 = \langle A_{0c} \rangle$	1
Friction coefficient	μ	1
Simulation box width	L_x	53.73
Simulation box length	L_y	55.84
Active region size	R	1–20
Box half-width active simulation	$W_{\text{half-box}}$	{20, 24, 14}
Medial activity parameter	λ_A	{0, 0.5}
Perimeter activity parameter	λ_P	{0, 0.1}
Integration time step	Δt	0.05

C Circular active patch

C.1 Ordinary differential equation system

We consider a tissue initially at equilibrium characterized by a uniform field \mathbb{M} , with $M(t=0) = m = A_0/c_1$, $c(t=0) = 0$ and $\theta(t=0) = 0$, which is subject to an active process that changes radially the target parameters as $A_0 \rightarrow A_0 + \Delta_A(\mathbf{r})$ and $P_0 \rightarrow$

$P_0 + \Delta_P(\mathbf{r})$, with $\Delta_A = -\lambda_A A_0 c \Gamma(r)$ and $\Delta_P = -\lambda_P P_0 c \Gamma(r)$. Here, $\Gamma(r) = \exp(-r^2/R^2)$ is the function that describes the active inhomogeneity in the tissue, where r is the radial coordinate measured from the center of the circular patch, and R represents the active region extension. Positive values for λ_A and λ_P cause apical contractions. In the case of a circular patch, the active stresses are given by $\sigma_{A_0} = -p_{A_0} \mathbb{1}$ and $\sigma_{P_0} = -p_{P_0} \mathbb{1} + \sigma_{P_0, \text{dev}}$, with pressures and the deviatoric stresses as in Eqs. (8), (9), and (10). Given the symmetries of our initial system, we assume a radial displacement field $\mathbf{u} = u_r(r) \hat{\mathbf{r}}$, with the coarse-grained orientations given by the θ -polar angle, and the scalar fields depending only on r , $M = M(r)$ and $c = c(r)$. Then, the confluence condition for the tissue [Eq. (3)], in polar coordinates, reads

$$M \begin{pmatrix} e^c & 0 \\ 0 & e^{-c} \end{pmatrix} = m \begin{pmatrix} 1 + 2 \frac{du_r}{dr} & 0 \\ 0 & 1 + 2 \frac{u_r}{r} \end{pmatrix}, \quad (21)$$

from where we obtain the following relations

$$M(r) = m \sqrt{\left(1 + 2 \frac{du_r}{dr}\right) \left(1 + 2 \frac{u_r}{r}\right)}, \quad (22)$$

$$\cosh[c(r)] = \frac{m}{M(r)} \left(\frac{du_r}{dr} + \frac{u_r}{r} + 1 \right) = \frac{\frac{du_r}{dr} + \frac{u_r}{r} + 1}{\sqrt{\left(1 + 2 \frac{du_r}{dr}\right) \left(1 + 2 \frac{u_r}{r}\right)}}, \quad (23)$$

$$\sinh[c(r)] = \frac{m}{M(r)} \left(\frac{du_r}{dr} - \frac{u_r}{r} \right) = \frac{\frac{du_r}{dr} - \frac{u_r}{r}}{\sqrt{\left(1 + 2 \frac{du_r}{dr}\right) \left(1 + 2 \frac{u_r}{r}\right)}}. \quad (24)$$

Since all the fields depend on the radial coordinate only, each stress term ($\sigma_i = \{\sigma_e, \sigma_{A_0}, \sigma_{P_0}\}$) generates a radial force

$$\nabla \cdot \sigma_i = \left(\frac{\partial \sigma_i^{rr}}{\partial r} + \frac{1}{r} [\sigma_i^{rr} - \sigma_i^{\theta\theta}] \right) \hat{\mathbf{r}} = f_i \hat{\mathbf{r}}, \quad (25)$$

where

$$\sigma_e^{rr} = K_A (c_1 M - A_0) + K_P \frac{c_2}{c_1} \left(c_2 - \frac{P_0 - J/(2K_P)}{\sqrt{2M \cosh[c(x)]}} \right) \sqrt{\frac{1 + 2 \frac{du_r}{dr}}{1 + 2 \frac{u_r}{r}}}, \quad (26)$$

$$\sigma_e^{\theta\theta} = K_A (c_1 M - A_0) + K_P \frac{c_2}{c_1} \left(c_2 - \frac{P_0 - J/(2K_P)}{\sqrt{2M \cosh[c(x)]}} \right) \sqrt{\frac{1 + 2 \frac{u_r}{r}}{1 + 2 \frac{du_r}{dr}}}. \quad (27)$$

Then, the equilibrium condition is written as $\sum_i f_i = 0$. Finally, we can write each force [Eq. (25)] in terms of r , $u_r(r)$, $u_r'(r)$, and $u_r''(r)$, obtaining an ordinary differential equation from the equilibrium condition. Analogous to the simple active stripe case, we numerically solve the equation considering the previously described initial condition, imposing $u_r(r=0) = 0$, $u_r(r = W_{\text{half-box}}) = 0$, and using $c_1 = 3\sqrt{3}/2$, $c_2 = 3\sqrt{2}$. To analyze the temporal evolution, we numerically solve

$$\frac{\mu}{A_v} \frac{\partial u_r(r,t)}{\partial t} = \sum_i f_i(r,t), \quad (28)$$

where $f_i = \{f_e, f_{A_0}, f_{P_0}\}$, $A_v = 1/2$, imposing $u_r(r, t=0) = 0$, $u_r(r = W_{\text{half-box}}, t) = 0$, and $u(r = W_{\text{half-box}}, t) = 0$.

C.2 Circular active patch: Results

Figure 8 shows the vertex displacement, change in the cellular area, and change in cellular perimeter, for an ordered tissue (regular hexagonal cells) of radius $W_{\text{half-box}} = 24$ under fixed boundary condition, with a circular region ($R = 6$) under medial activity defined by $\lambda_A = 0.5$, $\lambda_P = 0$. As in Fig. 1, we find that the results from continuum description depend on J (solid-black vs lime curve in Fig. 8D-E-F), in contrast to the numerical simulations for

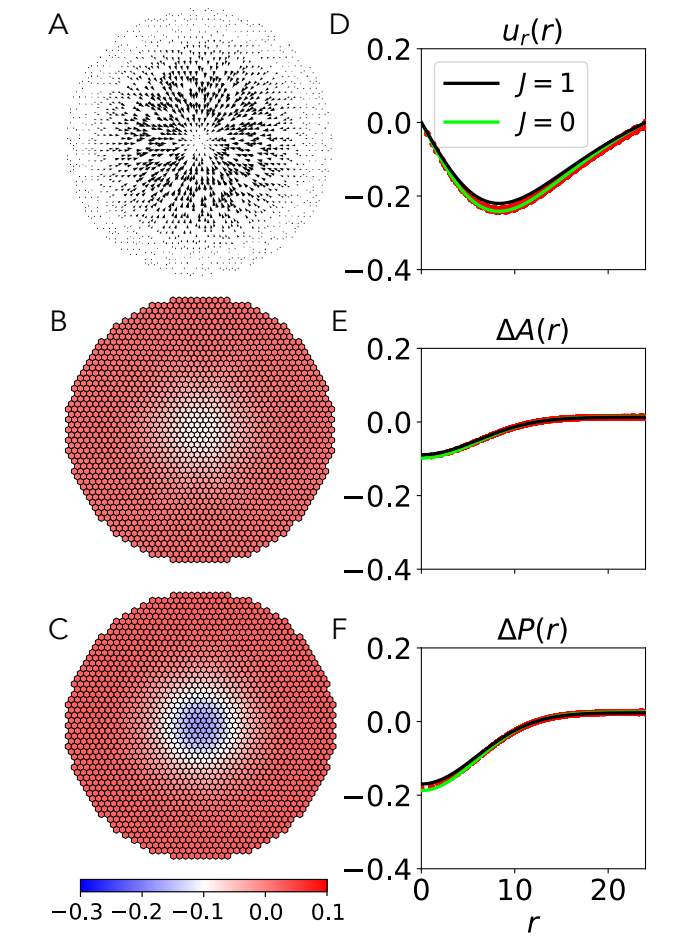


Fig. 8 Contraction of a circular active patch in an ordered tissue. Results of the simulated circular epithelial tissue, made from regular hexagonal cells, with a circular active patch under medial activity ($\lambda_A = 0.5$, $\lambda_P = 0$, $R = 6$, $P_0 = 3.72$, and $W_{\text{half-box}} = 24$) at $t = 100$, versus the initial position of the vertex or cell centers. (A) Vectorial map of total vertex displacement in the complete effective tissue, in units of $[\sqrt{A_0}/5]$. (B) Area change for the whole, effective tissue. (C) Perimeter change for the whole, effective tissue. (D) Scatter plot of the radial displacement of vertices (red dots). (E) Scatter plot of the area change (red dots). (F) Scatter plot of the perimeter change (red dots). The solid-black (lime) curves show the outcomes of the continuum description, using $J = 1$ ($J = 0$), $c_1 = 3\sqrt{3}/2$, $c_2 = 3\sqrt{2}$, $A_0 = 1$, and $P_0 = 3.72$.

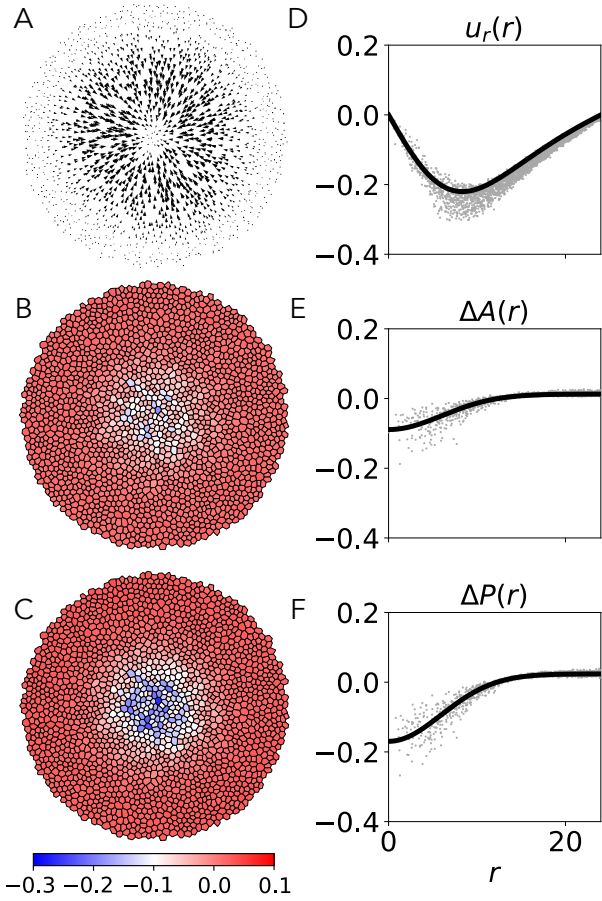


Fig. 9 Contraction of a circular active patch in a disordered tissue. Results of the simulated circular disordered epithelial tissue with a circular active patch under medial activity ($\lambda_A = 0.5$, $\lambda_P = 0$, $R = 6$, and $W_{\text{half-box}} = 24$) at $t = 100$, versus the initial position of the vertex or cell centers. (A) Vectorial map of total vertex displacement in the complete effective tissue, in units of $[\sqrt{A_0}/5]$. (B) Area change for the whole, effective tissue. (C) Perimeter change for the whole, effective tissue. (D) Scatter plot of the radial displacement of vertices. (E) Scatter plot of the area change. (F) Scatter plot of the perimeter change. The solid-black curves show the outcomes of the continuum description, using $c_1 = 3\sqrt{3}/2$, $c_2 = 3\sqrt{2}$, $A_0 = 1$, and $P_0 = 3.9$.

this high-symmetry case. Fig. 9 shows the analogous results when considering the disordered tissue. Vertices displacements are approximately in the radial direction, and geometrical changes in area and perimeter show large variations near the origin of the activity. Therefore, the maximum contraction is not well defined and is not considered as a relevant experimental observable to quantify. The results obtained from the continuum description, with $J = 0$, lie inside the gray data points obtained from numerical simulations using the two-dimensional vertex model.

Figure 10 shows the maximum vertex radial displacement and the radius at which it occurs (measured with respect to the origin of activity) in the final steady-state, considering medial activity with ($\lambda_A = 0.5$, $\lambda_P = 0$), and perimeter activity with ($\lambda_A = 0$, $\lambda_P = 0.1$) using the disordered tissue. The results obtained from the continuum description ($c_1 = 3\sqrt{3}/2$, and $c_2 = 3\sqrt{2}$) lie inside the error bars of the numerical simulations. Analog to the simple active stripe, the standard variation of the radial displacement at

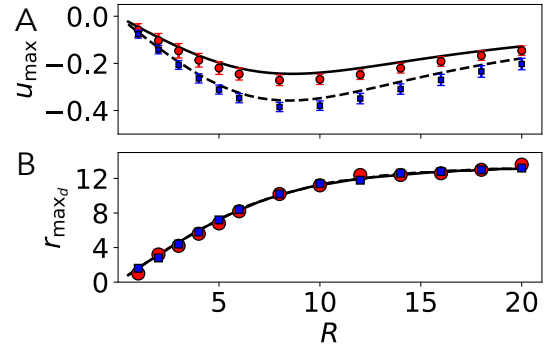


Fig. 10 Comparison of micro and macro descriptions of the steady-state. Results of the simulated circular disordered epithelial tissue with a circular active patch under circular activity ($R = 6$, $W_{\text{half-box}} = 24$). (A) Maximum horizontal displacement. (B) Radius at which the radial displacement is maximum. Black curves show the outcomes of the continuum description for medial ($\lambda_A = 0.5$, $\lambda_P = 0.0$) (solid-line) and perimeter ($\lambda_A = 0$, $\lambda_P = 0.1$) (dashed-line) activity. Red circles and blue squares represent the numerical results averaged over 100 simulations with different active origins for different integer R between 1 and 20. Bars show the standard deviations of u at the position of maximum displacement.

the position of maximum displacement is small and similar for both activities. Also, the position of maximum displacement is remarkably similar for both kinds of activity. Figure 11 shows the temporal evolution of the maximum vertex radial displacement, the radius at which it occurs, and its agreement with the continuum description (using $c_1 = 3\sqrt{3}/2$, $c_2 = 3\sqrt{2}$, and $\bar{\mu} = 2\mu$).

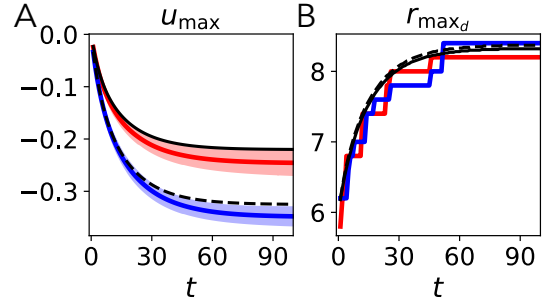


Fig. 11 Comparison of micro and macro descriptions of the tissue evolution in time. (A) Maximum horizontal displacement. (B) Radius at which the radial displacement is maximum. Black curves show the outcomes of the continuum description with $\bar{\mu} = 2\mu$ (hexagonal lattice), for medial ($\lambda_A = 0.5$, $\lambda_P = 0$, and $R = 6$) (solid-line) and perimeter ($\lambda_A = 0$, $\lambda_P = 0.1$, and $R = 6$) (dashed-line) activity. Solid-red and solid-blue curves represent the numerical mean results obtained from 100 simulations with different active axes. Shaded areas represent standard deviations of u_r at the radius of maximum displacement.

D Tissue made of square cells with a simple active stripe

As an additional test of the validity of the continuum description, we consider a tissue made of regular square cells, for which c_1 , c_2 , and $\bar{\mu}$ change in comparison with the case of hexagonal cells. Fig. 12 shows the vertex displacement, change in the cellular area, and change in the cellular perimeter for a tissue of size L_y and $W_{\text{half-box}} = 14$, made of square cells only. The tis-

sue is under horizontal fixed boundary conditions and vertical periodic boundary conditions. We consider an active stripe defined by $R = 3$ under medial activity with $\lambda_A = 0.5, \lambda_P = 0$, with $K_A = 1, K_P = 1$, and $J = 1$. Due to the high symmetry, vertices are horizontally displaced only, and there is no standard deviation for each quantity. As for the simulations shown in Figs. 1 and 8, here the value of J is irrelevant in the vertex model simulation due to the high symmetry. Fig. 12 shows the J -dependence of the continuum description. Overall, the agreement is excellent.

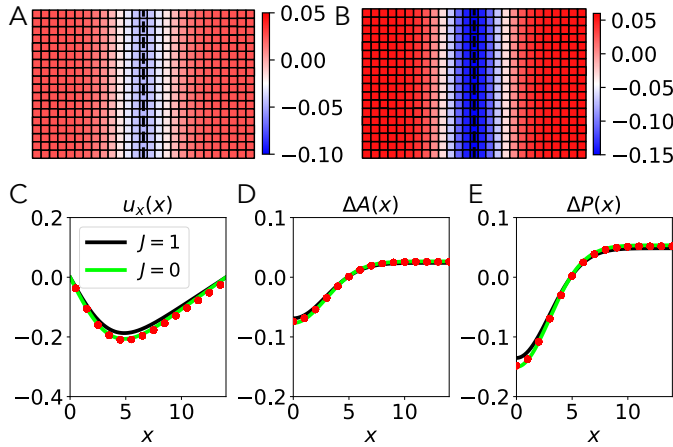


Fig. 12 Contraction of a simple active stripe: square cells. Results of the simulated epithelial tissue made of initially square cells of side equals one, with $K_A = 1, K_P = 1, A_0 = 1, P_0 = 4$, and $J = 1$, under medial activity ($\lambda_A = 0.5, \lambda_P = 0, R = 3$, and $W_{\text{half-box}} = 14$) at $t = 100$, versus the initial position of the vertex or cell centers. (A) Representative section of the tissue, showing area change. (B) Representative section of the tissue, showing perimeter change. (C) Scatter plot of the horizontal displacement of vertices (red dots). (D) Scatter plot of the area change (red dots). (E) Scatter plot of the perimeter change (red dots). The solid-black (lime) curves show the outcomes of the continuum description, with $J = 1$ ($J = 0$), $A_0 = 1, P_0 = 4, c_1 = 2, c_2 = 4$ (square cells).

Figure 13 shows the temporal evolution of the maximum contraction (which takes place at $x = 0$), the maximum vertex displacement, and the position at which it occurs, along with the continuum solution when using two values of J . Since cells are squares, we use $c_1 = 2, c_2 = 4$ in the continuum description. Also, since a square lattice has a ratio of cells over vertices of one, then $\bar{\mu} = \mu$.

Author Contributions

Conceptualization, F.P.-V. and R.S.; methodology, F.P.-V. and R.S.; software, F.P.-V.; validation, F.P.-V. and R.S.; formal analysis, F.P.-V. and R.S.; investigation, F.P.-V.; resources, R.S.; writing-original draft, F.P.-V. and R.S.; writing-review and editing, F.P.-V. and R.S.; supervision, R.S.; funding acquisition, R.S.

Conflicts of interest

There are no conflicts to declare.

Acknowledgements

We thank Shiladitya Banerjee for useful suggestions. This research was supported by the Fondecyt Grant No. 1220536 and

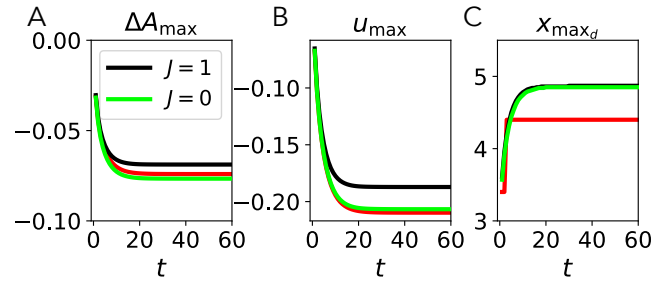


Fig. 13 Comparison of micro and macro descriptions of the tissue evolution in time. Results of the simulated epithelial tissue made of initially regular square cells of side one, with $K_A = 1, K_P = 1, A_0 = 1, P_0 = 4$, and $J = 1$, under medial activity ($\lambda_A = 0.5, \lambda_P = 0, R = 3, W_{\text{half-box}} = 14$) at $t = 100$. (A) Maximum contraction in time. (B) Maximum displacement in time. (C) Position at which the displacement is maximum in time. The solid-black (lime) curves show the outcomes of the continuum description, with $J = 1$ ($J = 0$), $A_0 = 1, P_0 = 4, c_1 = 2, c_2 = 4, \bar{\mu} = \mu$ (square lattice).

Millennium Science Initiative Program NCN19_170D of ANID, Chile.

Notes and references

- 1 J. M. Burke, C. M. Skumatz, P. E. Irving and B. S. McKay, *Experimental eye research*, 1996, **62**, 63–73.
- 2 W. C. Aird, *Cold Spring Harbor perspectives in medicine*, 2012, **2**, a006429.
- 3 N. Tonotsuka, Y. Hosoi, S. Miyazaki, G. Miyata, K. Sugawara, T. Mori, N. Ouchi, S. Satomi, Y. Matsumoto, K. Nakagawa *et al.*, *International journal of molecular medicine*, 2017, **18**, 441–447.
- 4 L. Lin and D.-C. Lin, *Cancers*, 2019, **11**, 1156.
- 5 A. A. Alizadeh, V. Aranda, A. Bardelli, C. Blanpain, C. Bock, C. Borowski, C. Caldas, A. Califano, M. Doherty, M. Elsner *et al.*, *Nature medicine*, 2015, **21**, 846–853.
- 6 M. Vishwakarma, B. Thurakkal, J. P. Spatz and T. Das, *Philosophical Transactions of the Royal Society B*, 2020, **375**, 20190391.
- 7 X. Li, A. Das and D. Bi, *Physical review letters*, 2019, **123**, 058101.
- 8 A. Gough, A. M. Stern, J. Maier, T. Lezon, T.-Y. Shun, C. Chennubhotla, M. E. Schurdak, S. A. Haney and D. L. Taylor, *Slas Discovery: Advancing Life Sciences R&D*, 2017, **22**, 213–237.
- 9 A. Tsuboi, D. Umetsu, E. Kuranaga and K. Fujimoto, *Frontiers in cell and developmental biology*, 2017, **5**, 68.
- 10 R. J. Murphy, P. R. Buenzli, R. E. Baker and M. J. Simpson, *Bulletin of Mathematical Biology*, 2020, **82**, 130.
- 11 F. Pérez-Verdugo, G. Reig, M. Cerda, M. L. Concha and R. Soto, *Journal of the Royal Society Interface*, 2022, **19**, 20210851.
- 12 S. Ishihara, P. Marcq and K. Sugimura, *Physical Review E*, 2017, **96**, 022418.
- 13 P. Spahn and R. Reuter, *PLoS One*, 2013, **8**, e75051.
- 14 N. C. Heer, P. W. Miller, S. Chanet, N. Stoop, J. Dunkel and A. C. Martin, *Development*, 2017, **144**, 1876–1886.

- 15 Y. Inoue, M. Suzuki, T. Watanabe, N. Yasue, I. Tateo, T. Adachi and N. Ueno, *Biomechanics and modeling in mechanobiology*, 2016, **15**, 1733.
- 16 T. Nagai, K. Kawasaki and K. Nakamura, *Journal of the physical society of Japan*, 1988, **57**, 2221–2224.
- 17 T. Nagai and H. Honda, *Philosophical Magazine B*, 2001, **81**, 699.
- 18 R. Farhadifar, J.-C. Röper, B. Aigouy, S. Eaton and F. Jülicher, *Current Biology*, 2007, **17**, 2095.
- 19 A. G. Fletcher, M. Osterfield, R. E. Baker and S. Y. Shvartsman, *Biophysical journal*, 2014, **106**, 2291.
- 20 J. Kursawe, P. A. Brodskiy, J. J. Zartman, R. E. Baker and A. G. Fletcher, *PLoS computational biology*, 2015, **11**, e1004679.
- 21 K. Sato and D. Umetsu, *Frontiers in Physics*, 2021, **9**, 704878.
- 22 A. Nestor-Bergmann, G. Goddard, S. Woolner and O. E. Jensen, *Mathematical medicine and biology: a journal of the IMA*, 2018, **35**, i1–i27.
- 23 D. Grossman and J.-F. Joanny, *Physical Review Letters*, 2022, **129**, 048102.
- 24 A. Hernandez, M. F. Staddon, M. J. Bowick, M. C. Marchetti and M. Moshe, *Physical Review E*, 2022, **105**, 064611.
- 25 A. C. Martin and B. Goldstein, *Development*, 2014, **141**, 1987–1998.
- 26 Y. Atieh, T. Wyatt, A. M. Zaske and G. T. Eisenhoffer, *Current Biology*, 2021, **31**, 1129–1140.
- 27 A. C. Martin, *Genetics*, 2020, **214**, 543–560.
- 28 G. Reig, M. Cerda, N. Sepúlveda, D. Flores, V. Castaneda, M. Tada, S. Härtel and M. L. Concha, *Nature communications*, 2017, **8**, 1–14.
- 29 S. Okuda, K. Unoki, M. Eiraku and K.-i. Tsubota, *Development, Growth & Differentiation*, 2017, **59**, 455–464.
- 30 D. Bi, J. Lopez, J. M. Schwarz and M. L. Manning, *Nature Physics*, 2015, **11**, 1074.
- 31 L. D. Landau, E. M. Lifshitz, A. M. Kosevich and L. P. Pitaevskii, *Theory of elasticity: volume 7*, Elsevier, 1986, vol. 7.
- 32 C. Bielmeier, S. Alt, V. Weichselberger, M. La Fortezza, H. Harz, F. Jülicher, G. Salbreux and A.-K. Classen, *Current Biology*, 2016, **16**, 563–574.
- 33 F. Pérez-Verdugo, J.-F. Joanny and R. Soto, *Physical Review E*, 2020, **102**, 052604.
- 34 J.-A. Park, J. H. Kim, D. Bi, J. A. Mitchel, N. T. Qazvini, K. Tantisira, C. Y. Park, M. McGill, S.-H. Kim, B. Gweon *et al.*, *Nature materials*, 2015, **14**, 1040–1048.
- 35 X. Wang, M. Merkel, L. B. Sutter, G. Erdemci-Tandogan, M. L. Manning and K. E. Kasza, *Proceedings of the National Academy of Sciences*, 2020, **117**, 13541–13551.
- 36 O. K. Damavandi, E. Lawson-Keister and M. L. Manning, *bioRxiv*, 2022, 2022.06.01.494406.